research papers

Investigation of the damping wiggler effect and application on the PAL fourth-generation storage ring

Gyeongsu Jang,[a] M. Yoon,[a] J. Lee,[b] B.-H. Oh,[b] J. Kim,[c] D.-E. Kim[c,b] and S. Shin[b]*

[a]Department of Physics, POSTECH, Pohang, Gyungbuk 37673, South Korea, [b]Pohang Accelerator Laboratory, POSTECH, Pohang, Gyungbuk 37673, South Korea, and [c]SLAC National Accelerator Laboratory, Menlo Park, CA 94025, USA. *Correspondence e-mail: tlssh@postech.ac.kr

An investigation of the damping wiggler effect to reduce the emittance in the Pohang Accelerator Laboratory (PAL), a fourth-generation storage ring (4GSR) that uses a multi-bend achromat, is presented. A 4GSR lattice which has reduced emittance and increased dynamic aperture to amplify the synergy with two existing light sources (PLS-II and PAL-XFEL) at PAL is described.

1. Introduction

A fourth-generation storage ring (4GSR) that uses the multi-bend achromat (MBA) lattice concept may be able to surpass the brightness and coherence that are attained using present third-generation storage rings (3GSRs). 4GSRs are part of a world-wide effort to exceed the brightness and coherence reached by present 3GSRs. MAX IV (MAX IV, 2020) was the first MBA machine; the next, Sirius (Liu *et al.*, 2013), is currently under construction. Other projects are being conducted to convert existing 3GSRs such as ESRF, APS, SPring-8 and ALS (Revol, 2017; APS, 2020; SPring-8, 2014; Steier *et al.*, 2016) to 4GSRs. These modifications will reduce beam emittance to a few hundred picometres, or even to ≤ 100 pm, but many efforts have been made to reduce the natural emittance further. The natural emittance in an electron storage ring is given by

$$\varepsilon_0 = C_q \gamma^2 \frac{\langle \mathcal{H}/|\rho^3| \rangle}{j_x \langle 1/\rho^2 \rangle}, \qquad (1)$$

where C_q is a constant (for electrons $C_q \simeq 3.832 \times 10^{-13}$ m), γ is the relativistic factor for a particle, $\mathcal{H} \simeq 1/\rho^2$ (where ρ is the unit-cell bending angle) and j_x is the horizontal damping partition number (Borland *et al.*, 2014). The natural emittance scales with the inverse cube of ρ, so MBA lattices enable emittance reduction by one to two orders of magnitude compared with third-generation light sources.

The advent of 4GSRs enables a ring free-electron laser (FEL) to perform high-average-power extreme ultraviolet lithography (Luong, 2018) due to its ability to generate extremely low electron beam emittance. However, 4GSRs still have limitations such as relatively large energy spread and low repetition rate in FELs in the bypass line from the storage ring. A method to compensate for the effects of beam energy spread by introducing a transverse variation of the undulator magnetic field has been proposed (Huang *et al.*, 2012), but the average power of the photon beam is insufficient because of
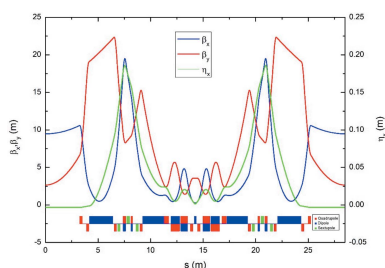
the low repetition rate in a ring FEL that uses a bypass line (Cai *et al.*, 2013). To further reduce the emittance, the concepts of the longitudinal gradient bend and reverse bends have been considered for a lattice design to achieve sub-theoretical minimum emittance (Riemann & Streun, 2019). Use of a damping wiggler is an option to reduce emittance further, and its effect should be explored. The damping wiggler increases the repetition rate of the FEL beam by reducing the damping time; this effect must be quantified.

Recently a 4GSR has been designed at the Pohang Accelerator Laboratory (PAL-4GSR) using concepts from ESRF-EBS and APS-U. As a result, a lattice with 3 GeV energy and 90 pm emittance with a 570 m ring was proposed. We investigate the effect of a damping wiggler on PAL-4GSR, particularly focusing on emittance reduction and repetition rate increase. In this paper, we describe the PAL-4GSR lattice, and the overall damping-wiggler effect on PAL-4GSR. Section 2 describes the lattice design and beam dynamics studies for PAL-4GSR. Section 3 presents derivation of analytic formulas for the damping wiggler effect on beam parameters. Section 4 applies the analytic formulas to PAL-4GSR and compares them with simulations conducted using *Elegant* software (Borland, 2000). Section 5 presents a summary and concluding remarks.

2. PAL-4GSR

The PAL-4GSR storage ring (Table 1) is a hybrid seven-bend achromat lattice with a horizontal emittance of 90 pm. The ring is 570 m in circumference and is composed of 20 symmetrical cells. The length of the straight section is set as 6.5 m to accommodate two superconducting RF modules, as a result of experience on PLS-II (Shin *et al.*, 2013). The PAL-4GSR lattice contains a 2 T super-bend in the central dipole to produce radiation with a critical energy of 12 keV (Fig. 1).

The concepts of the ESRF-EBS and APS-U lattices were adopted in the PAL-4GSR lattice. The dispersion was deliberately enlarged between the first and second dipoles and between the sixth and seventh dipoles, and chromatic sextu-

Table 1
Main parameters of the PAL-4GSR.

Parameter	Value	Unit
Energy	3	GeV
Emittance (flat / round)	89.4 / 58	pm
Circumference	570	m
Tune (x / y)	48.380 / 17.376	–
Natural chromaticity (x / y)	-95.97 / -57.91	–
Radiation loss per turn	0.468 (without ID)	MeV
Momentum compaction	1.45×10^{-4}	
Damping partition (H / V / L)	1.82 / 1.00 / 1.18	
Damping time (H / V / L)	13.37 / 24.35 / 20.66	ms

poles have been placed in this dispersion-bump region to reduce the strength required to control the chromaticity. The betatron phase advances between the two dispersion bumps were set to $\Delta\varphi_x \simeq 3\pi$ in the horizontal plane and $\Delta\varphi_y \simeq \pi$ in the vertical plane. As a result, nonchromatic effects of the sextupoles are canceled naturally to first order. To minimize natural emittance, five-step longitudinal gradient dipoles and reverse bending magnets were considered.

The sextupoles are two-cell periodic in order to increase the number of control knobs. Therefore, a total of ten sextupoles in two cells, except two sextupoles for correcting the linear chromaticity (Fig. 2), are used in the optimization with a multi-objective genetic algorithm (MOGA) (Deb, 2001). The objectives are an on-momentum dynamic aperture for off-axis beam injection and an off-momentum dynamic aperture (4%) to extend the Touschek lifetime. The result (Fig. 3) of MOGA optimization seems to have converged after 150 generations, at which the strengths of ten harmonic sextupoles reach a compromise between on-momentum dynamic aperture and 4% off-momentum dynamic aperture. The candidate point for the studies (marked by the star in Fig. 3) has a maximum on-momentum dynamic aperture area among the flat region for the off-momentum dynamics aperture area. As a result, large dynamic apertures were attained, enough for the off-axis injection with random errors (Fig. 4). Here, 30 μm r.m.s. offset, 200–500 μrad r.m.s. rotation and 0.1–0.2% r.m.s. field errors are assumed to generate 100 random errors. Despite assuming this harmful error scenario, a horizontal dynamic aperture from -9 mm to 12 mm is promising for 6 mm off-axis beam injection.

To obtain maximum Touschek lifetime, the RF voltage is scanned in the particle tracking with the optimized sextupole configuration (Fig. 5). At 3.1 MV RF voltage, which corre-
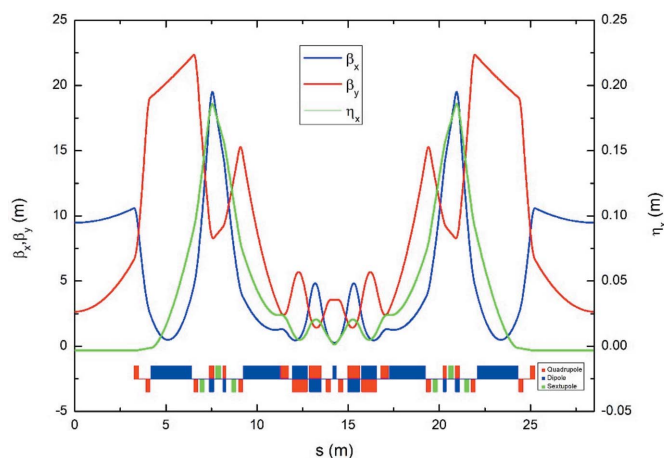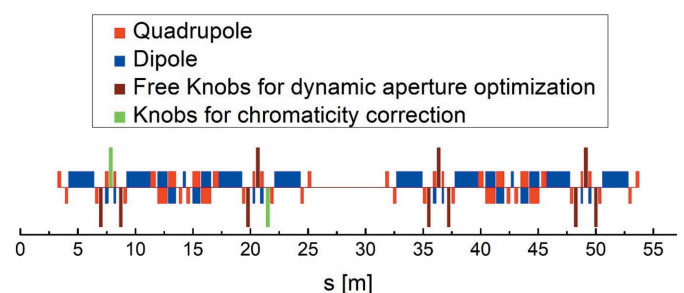

Figure 1
Lattice functions for PAL-4GSR.

Figure 2
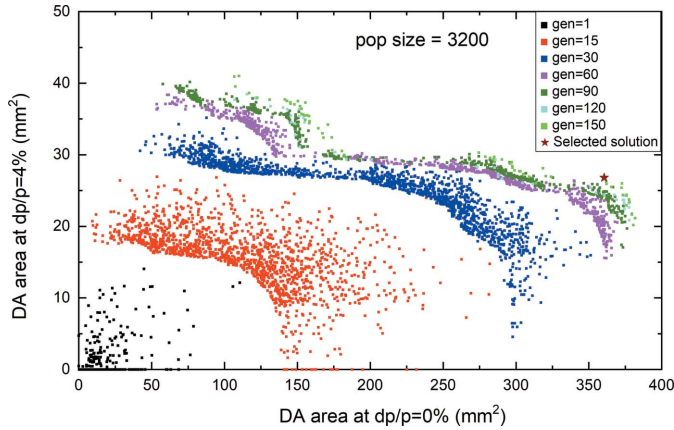Configuration of sextupoles and other magnetic elements in two cells.

Figure 3
MOGA optimization for large dynamic aperture area. The star on the Pareto front shows the candidate point for the studies; it has a maximum on-momentum dynamic aperture area among the flat region for the off-momentum dynamics aperture area.
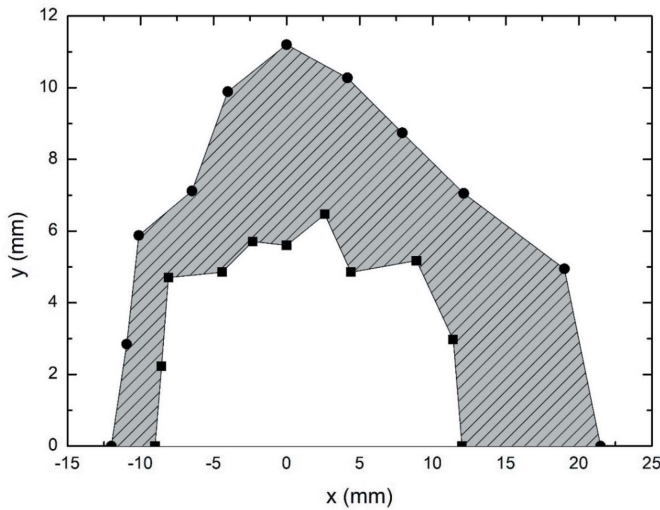

Figure 4
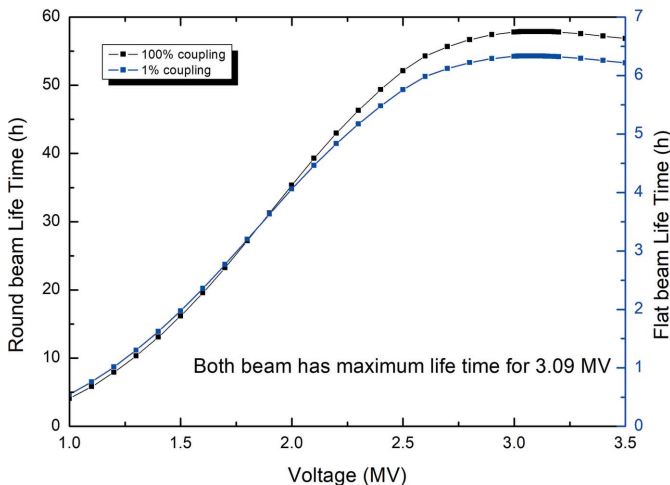Dynamic aperture with errors for beam injection.

Figure 5
Touschek lifetime along RF voltage. At 3.1 MV RF voltage, Touschek lifetimes are 6 h for 1% coupling flat beam and 58 h for round beam.
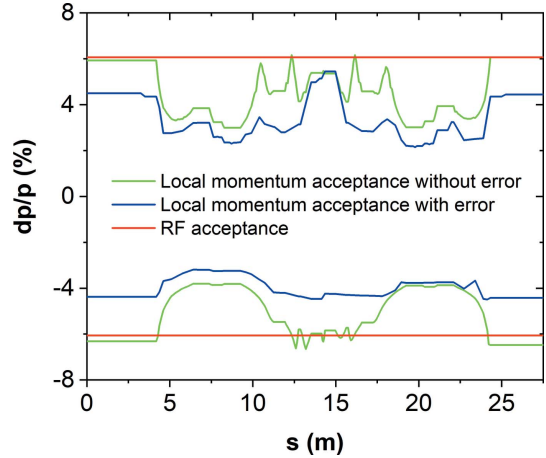

Figure 6
Local momentum acceptance. Green line: lattice acceptance without error; blue line: lattice acceptance with error; red line: RF acceptance.

sponds to 6% RF acceptance, Touschek lifetimes are 6 h for 1% coupling flat beam and 58 h for coupling round beam. Local momentum aperture tracking including error distributions is also compared with ideal local momentum aperture and RF momentum aperture (Fig. 6). Evaluated Touschek lifetimes in realistic conditions are 1.3 h for 1% coupling flat beam and 9.7 h for round beam at 1.9 MV optimum RF voltage, which corresponds to 4.3% RF acceptance. These lifetime reductions invoke the need of a harmonic cavity. Note that bunch lengthening from 3.45 mm r.m.s. to 20 mm r.m.s. with a harmonic cavity enables Touschek lifetimes to be increased up to 7 h for 1% coupling flat beam and 51 h for round beam. Here the factor 5.8 of bunch lengthening from the higher harmonic cavity is assumed to obtain sufficient lifetime in hybrid fill pattern operation with high single bunch current. In addition to the Touschek lifetime, the elastic scattering lifetime is 61 h, assuming a minimum half physical aperture of 2 mm, and the bremsstrahlung lifetime is 79 h.

The results of *Elegant* simulation of intra-beam scattering (Fig. 7) show a change in the zero-charge emittance along beam energy, which scales as $\sim E^2$. In the simulation, the algorithm uses the Bjorken & Mtingwa formula (Bjorken & Mtingwa, 1983) to simulate the intra-beam scattering (IBS) effect. For a 0.845 nC bunch, which is a single bunch current for a 400 mA multi-bunch, round beam operation must be used to avoid a large emittance increase due to the IBS effect. In addition, a harmonic cavity can be considered for bunch lengthening up to 20 mm. Here, the natural bunch length is 3.45 mm and the lengthening factor with harmonic cavity is 5.8.

3. Analytic formulas for the damping wiggler effect

In an electron storage ring, representative ring parameters can be expressed using synchrotron radiation integrals
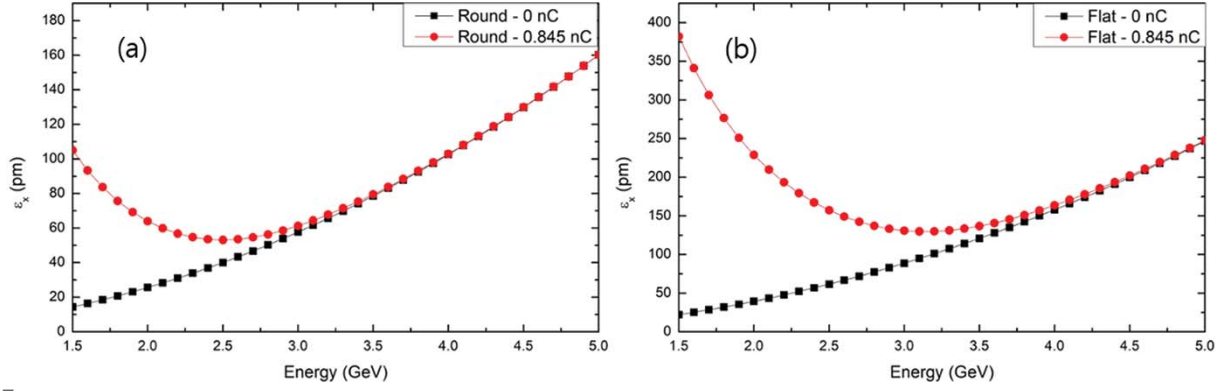
$$\epsilon_x = C_q \gamma^2 \frac{I_5}{I_2 - I_4},$$ (2)

Figure 7
Emittance along beam energy. (*a*) Round beam (100% coupling). (*b*) Flat beam (1% coupling).

$$\sigma_\delta^2 = C_q \gamma^2 \frac{I_3}{2I_2 + I_4}, \tag{3}$$

$$U_0 = \frac{C_\gamma}{2\pi} E^4 I_2, \tag{4}$$

$$\tau_x = \frac{4\pi T_0}{C_\gamma E^3 (I_2 - I_4)}, \tag{5}$$

$$\tau_y = \frac{2\pi T_0}{C_\gamma E^3 I_2}, \tag{6}$$

$$\tau_\delta = \frac{4\pi T_0}{C_\gamma E^3 (2I_2 + I_4)}, \tag{7}$$

$$\alpha_c = \frac{I_1}{C}, \tag{8}$$

where $C_q \simeq 3.84 \times 10^{-13}$ m, $C_\gamma \simeq 8.846 \times 10^{-5}$ m GeV^{-3}, ϵ_x is the natural horizontal emittance, E is the electron energy and τ is the damping time. The definition of the synchrotron radiation integral is given by

$$I_1 = \oint^{\mathrm{d}} s \left\{ \frac{\eta}{\rho} \right\},$$

$$I_2 = \oint^{\mathrm{d}} s \left\{ \frac{1}{\rho^2} \right\},$$

$$I_3 = \oint^{\mathrm{d}} s \left\{ \frac{\eta}{|\rho|^3} \right\}, \tag{9}$$

$$I_4 = \oint^{\mathrm{d}} s \left\{ \frac{\eta}{\rho} \left(\frac{1}{\rho^2} + 2k_1 \right) \right\},$$

$$I_5 = \oint^{\mathrm{d}} s \left\{ \frac{H}{|\rho|^3} \right\},$$

where $k_1 = (1/B\rho)(\partial B_y/\partial x)$, $H = \gamma\eta^2 + 2\alpha\eta\eta' + \beta\eta'^2$ (Wiedemann, 1993), and ρ is the curvature of a reference particle. These integrals are changed by considering a damping wiggler that has a vertical magnetic field given by

$$B_y = B_{\mathrm{w}} \sin k_{\mathrm{w}} s, \tag{10}$$

where $B_{\mathrm{w}} = B\rho/\rho_{\mathrm{w}}$ is the peak field, $k_{\mathrm{w}} = 2\pi/\lambda_{\mathrm{w}}$ is the wavenumber, and λ_{w} is the wiggler period. For the 3 GeV electron storage ring, the magnet rigidity $B\rho$ is ~ 10 T m. The synchrotron radiation integrals for the wiggler in the straight section are (Appendix *A*)

$$I_{1,\mathrm{wig}} = -\frac{\lambda_{\mathrm{w}}^2 B_{\mathrm{w}}^2 L_{\mathrm{w}}}{8\pi^2 \times 10^2},$$

$$I_{2,\mathrm{wig}} = \frac{B_{\mathrm{w}}^2 L_{\mathrm{w}}}{2 \times 10^2},$$

$$I_{3,\mathrm{wig}} = \frac{4 B_{\mathrm{w}}^3 L_{\mathrm{w}}}{3\pi \times 10^3}, \tag{11}$$

$$I_{4,\mathrm{wig}} = -\frac{3\lambda_{\mathrm{w}}^2 B_{\mathrm{w}}^4 L_{\mathrm{w}}}{32\pi^2 \times 10^4},$$

$$I_{5,\mathrm{wig}} = \frac{\langle \beta_x \rangle \lambda_{\mathrm{w}}^2 B_{\mathrm{w}}^5 L_{\mathrm{w}}}{15\pi^3 \times 10^5},$$

where L_{w} is the length of the wiggler and β_x is a horizontal beta-function. Equation (11) applies to a sinusoidal wiggler field versus s, but in reality the field of a long-period insertion device (ID) includes high harmonics of k_{w}.

The emittance ratio between the storage ring emittances without and with wiggler is given by

$$\frac{\epsilon_{\mathrm{tot}}}{\epsilon_{\mathrm{ring}}} = \frac{C_q \gamma^2 \frac{I_{5,\mathrm{tot}}}{I_{2,\mathrm{tot}} - I_{4,\mathrm{ring}}}}{C_q \gamma^2 \frac{I_{5,\mathrm{ring}}}{I_{2,\mathrm{ring}} - I_{4,\mathrm{ring}}}} = \frac{C_q \gamma^2 \frac{I_{5,\mathrm{ring}} + I_{5,\mathrm{wig}}}{I_{2,\mathrm{ring}} + I_{2,\mathrm{wig}} - I_{4,\mathrm{ring}} - I_{4,\mathrm{wig}}}}{C_q \gamma^2 \frac{I_{5,\mathrm{ring}}}{I_{2,\mathrm{ring}} - I_{4,\mathrm{ring}}}}$$

$$= \frac{1 + \frac{I_{5,\mathrm{wig}}}{I_{5,\mathrm{ring}}}}{1 + \frac{I_{2,\mathrm{wig}} - I_{4,\mathrm{wig}}}{I_{2,\mathrm{ring}} - I_{4,\mathrm{ring}}}} \tag{12}$$

where

$$I_{4,\mathrm{wig}} = -\frac{\lambda_{\mathrm{w}}^2 B_{\mathrm{w}}^2}{16\pi^2 \times 10^2} I_{2,\mathrm{wig}},$$

which is very small compared with $I_{2,\mathrm{wig}}$, so $I_{4,\mathrm{wig}}$ can be neglected for typical wiggler values in equation (12). The emittance ratio without $I_{4,\mathrm{wig}}$ becomes

$$\frac{\epsilon_{\text{tot}}}{\epsilon_{\text{ring}}} = \frac{1 + bL_{\text{w}}}{1 + aL_{\text{w}}}, \qquad (13)$$

where

$$a \equiv \frac{B_{\text{w}}^2}{2(I_{2,\text{ring}} - I_{4,\text{ring}}) \times 10^2}$$

and

$$b \equiv \frac{\langle\beta_x\rangle\lambda_{\text{w}}^2 B_{\text{w}}^5}{15\pi^3 I_{5,\text{ring}} \times 10^5}.$$

The form of the function $(1 + bL_{\text{w}})/(1 + aL_{\text{w}})$ depends on the ratio of a and b, which are always positive. $\epsilon_{\text{tot}}/\epsilon_{\text{ring}} = 1$ for $a = b$, $\epsilon_{\text{tot}}/\epsilon_{\text{ring}} = >1$ for $a < b$, and $\epsilon_{\text{tot}}/\epsilon_{\text{ring}} < 1$ for $a > b$. Here our main interest is the case of $\epsilon_{\text{tot}}/\epsilon_{\text{ring}} = <1$. When $a = 1.389B_{\text{w}}^2$ and $b = 0.486B_{\text{w}}^5$ the emittance ratio (Fig. 8) along the length of a damping wiggler is limited on the asymptotic line given by b/a, despite the extremely long wiggler length. Therefore, short wiggler period, small horizontal beta-function, long wiggler length and low magnetic field are favorable conditions to reduce total emittance when the wiggler is infinitely long. Minimum emittance reduction ratio along natural storage ring emittance (Fig. 9) implies that the emittance reduction by a damping wiggler is not so effective when natural storage-ring emittance is extremely small.

In the same manner, the ratios of energy spread, damping time and momentum compaction factor are also formulated as (Helm *et al.*, 1973)

$$\frac{\sigma_{\delta,\text{tot}}^2}{\sigma_{\delta,\text{ring}}^2} = \frac{1 + dL_{\text{w}}}{1 + cL_{\text{w}}}, \qquad (14)$$

where

$$c \equiv \frac{B_{\text{w}}^2}{(2I_{2,\text{ring}} + I_{4,\text{ring}}) \times 10^2} \quad \text{and} \quad d \equiv \frac{4B_{\text{w}}^3}{3\pi I_{3,\text{ring}} \times 10^3}$$
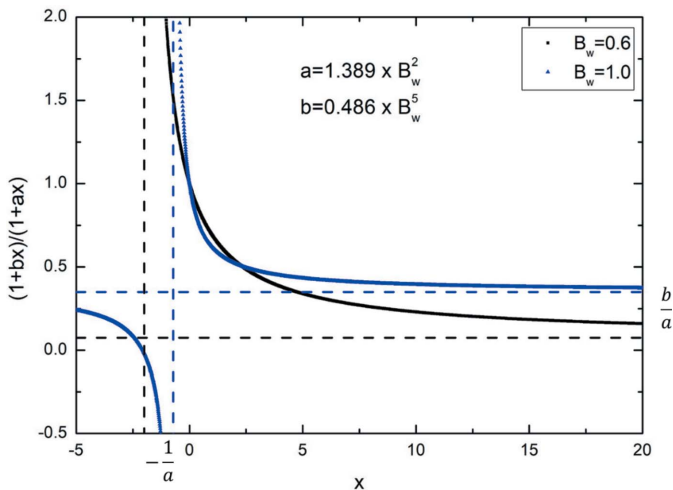

Figure 8
Emittance ratio with the function of wiggler length.

Table 2
Synchrotron radiation integrals for the PAL-4GSR.

Parameter	Value	Unit
$I_{1,\text{ring}}$	9.251×10^{-2}	m
$I_{2,\text{ring}}$	4.108×10^{-1}	m^{-1}
$I_{3,\text{ring}}$	4.254×10^{-1}	m^{-2}
$I_{4,\text{ring}}$	-3.317×10^{-1}	m^{-1}
$I_{5,\text{ring}}$	6.068×10^{-6}	m^{-1}

$$\frac{\tau_{\text{tot}}}{\tau_{\text{ring}}} = \frac{1}{1 + eL_{\text{w}}}, \qquad (15)$$

where

$$e_x \equiv \frac{B_{\text{w}}^2}{2(I_{2,\text{ring}} - I_{4,\text{ring}}) \times 10^2} \quad \text{and} \quad e_y \equiv \frac{B_{\text{w}}^2}{2I_{2,\text{ring}} \times 10^2} \quad \text{and}$$

$$e_\delta \equiv \frac{B_{\text{w}}^2}{(2I_{2,\text{ring}} + I_{4,\text{ring}}) \times 10^2},$$

$$\frac{\alpha_{c,\text{tot}}}{\alpha_{c,\text{ring}}} = 1 - fL_{\text{w}} \quad \text{where} \quad f \equiv \frac{\lambda_{\text{w}}^2 B_{\text{w}}^2}{8\pi^2 \alpha_{c,\text{ring}} c \times 10^2}. \qquad (16)$$

The equation for energy spread ratio has a similar form to that of the emittance ratio. Energy spread reduction is also limited by an asymptotic line. Damping time is always reduced by the damping wiggler and the reduction of momentum compaction factor is negligible because f in equation (16) is small.

4. Application on PAL-4GSR

The damping wiggler effects on the main beam parameters in the lattice of PAL-4GSR were investigated using the analytic formulae derived in Section 3 and the *Elegant* simulation. Four straight sections among a total of 20 straight sections are considered for each 4.5 m-long damping wiggler. In this case, four ID straight sections should be sacrificed for insertion of damping wigglers. The synchrotron radiation integrals (Table 2) for PAL-4GSR were obtained using simulation in *Elegant*. The theoretical results were also compared with the results of the *Elegant* simulation.
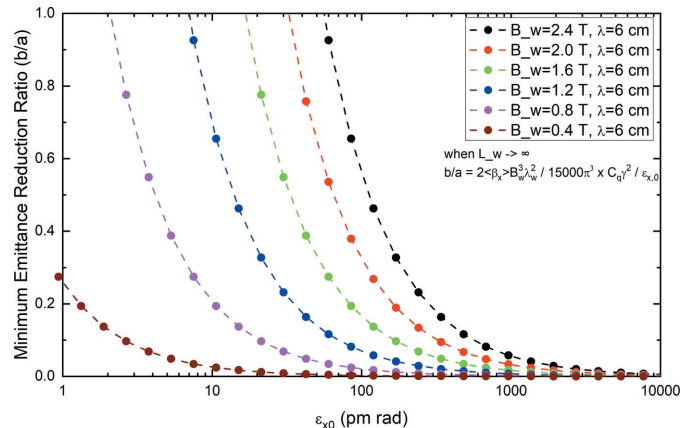

Figure 9
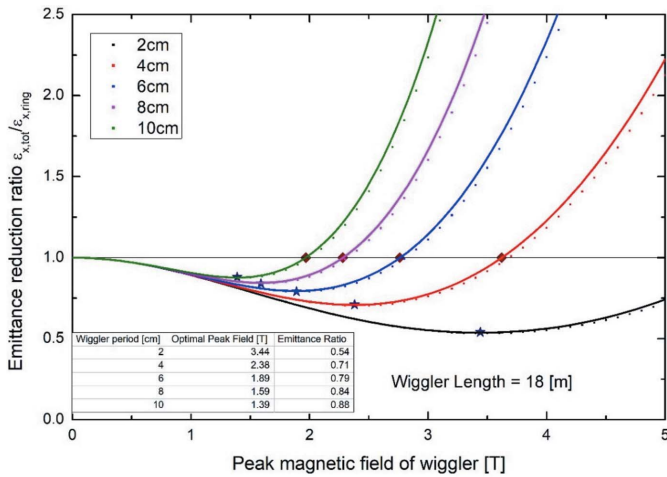Minimum emittance reduction ratio versus natural storage ring emittance.

Figure 10
Emittance change by using a damping wiggler. Dots: simulation results; lines: function plot; stars: optimal combination.

Figure 12
Reduction of damping times. Lines: damping time ratio plot; dots: simulation results. Red: horizontal damping time; blue: vertical damping time; green: longitudinal damping time.

Assuming a damping wiggler that had a total length of 18 m, the emittance-reduction ratios were investigated by scanning the wiggler period and the wiggler peak field (Fig. 10). The function plot from theoretical results agreed well with the simulation result obtained using *Elegant*. For a given wiggler period and wiggler length, an optimal wiggler peak field achieves the smallest emittance-reduction ratio (Fig. 10, stars); this peak field increases as the wiggler period decreases.

The allowable peak field should be obtained for a given short wiggler period. The Halbach formula was used to determine the optimal wiggler field along the wiggler period and magnetic field versus wavelength (Fig. 11). For the total 18 m wiggler length in PAL-4GSR, the minimum emittance reduction ratio is at most ~0.83. As already shown in Fig. 9,
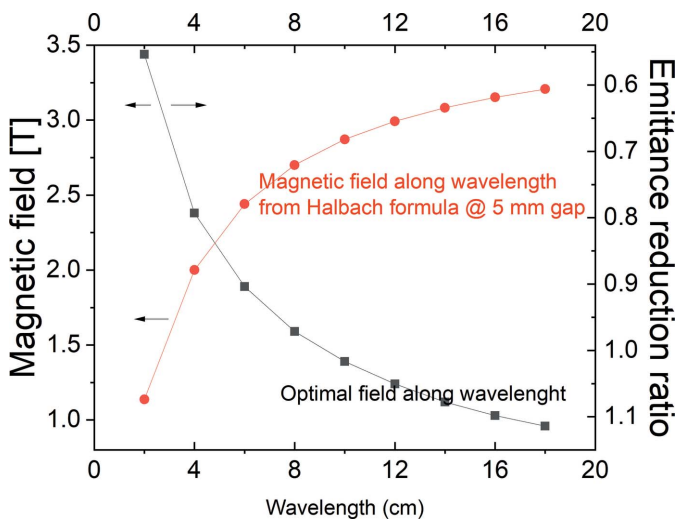

Figure 13
Energy spread versus magnetic peak field. The critical field that makes energy spread >1 is ~2 T.

emittance reduction by the damping wiggler is not so effective due to the small natural emittance.

For the FEL option through the bypass line, damping-time reduction was also investigated to estimate the increase of repetition rate for high average FEL power. Horizontal, vertical and longitudinal damping times have the same form; the only difference is in the coefficients [equation (15)]. The coefficients are independent of the wiggler period. In PAL-4GSR, they are

$$e_x = 6.73 \times 10^{-3} B_w^2,$$
$$e_y = 1.22 \times 10^{-2} B_w^2, \quad (17)$$
$$e_\delta = 2.04 \times 10^{-2} B_w^2.$$

Figure 11
Optimum magnetic field along wiggler period at a given total wiggler length from Fig. 10. Black line: effect of wiggler period on wiggler magnetic field, calculated using the Halbach formula at the given minimum gap of 5 mm. The region above the red line indicates a minimum gap < 5 mm.
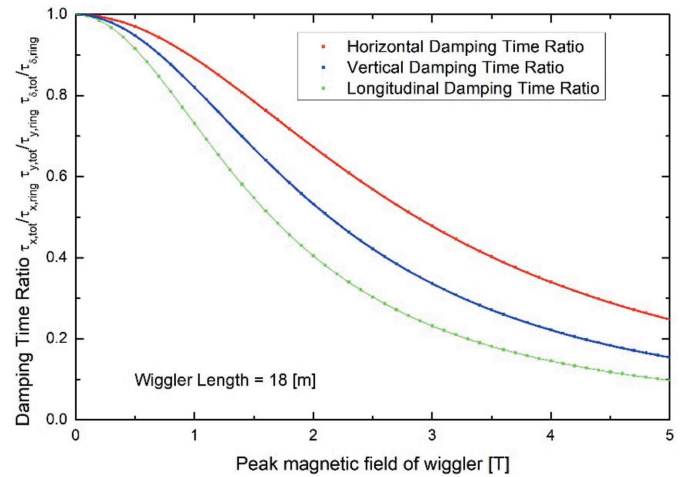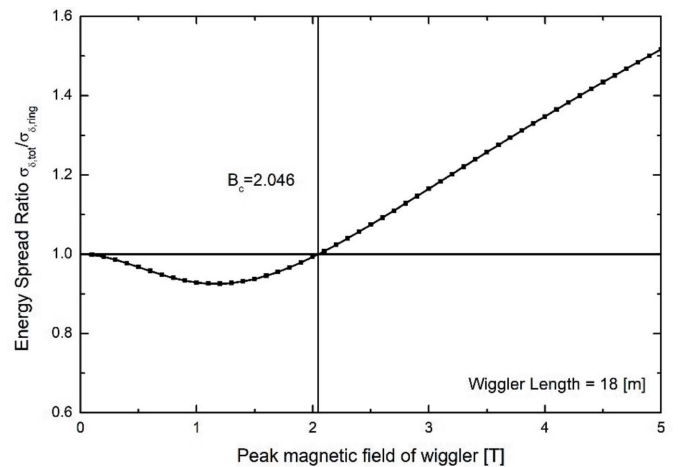
The damping-time reduction (Fig. 12) by a wiggler was calculated. A half-damping time (or double repetition rate) can be expected in a magnetic field >2.5 T. Similarly, the energy spread reduction can also be estimated (Fig. 13); an increase in energy spread is inevitable in a magnetic field >2 T.

These results show that the damping wiggler does not have much effect on the increase of ring FEL power.

5. Conclusion

Analytic analysis and *Elegant* simulation were performed to quantify the damping wiggler effects on PAL-4GSR which is a 3 GeV and 90 pm natural emittance storage ring with 570 m circumference. Analytic analysis agreed well with *Elegant* simulation, and described reductions in energy spread, damping time, and emittance. Emittance reduction by the damping wiggler was less effective than in third-generation storage rings due to the small natural emittance in the fouth-generation storage ring. Application of a damping wiggler on a ring FEL was also investigated in the aspect of increasing average brightness. Unfortunately the damping wiggler causes an increase in energy spread, and therefore cannot considerably increase the ring-FEL power.

APPENDIX A
Synchrotron radiation integrals

Helm *et al.* (1973) evaluated the synchrotron radiation integrals. Synchrotron integrals in the damping wiggler have been investigated by many authors (Katoh & Kamiya, 1987; Wiedemann, 1988; Walker, 1995). This section presents specific details of the damping wiggler's contribution to synchrotron integrals.

Synchrotron integrals are described using η, k_1 and $1/\rho$. Therefore, to obtain synchrotron integrals in the damping wiggler, the form of η, k_1 and $1/\rho$ in the damping wiggler should be realized. First, we obtained the dispersion function; assuming that the damping wiggler has a simple harmonic vertical field given by

$$B_y = B_w \sin k_w z, \tag{18}$$

where B_w is the peak wiggler field and $k_w = 2\pi/\lambda_w$, with λ_w being the wavelength of the damping wiggler, a Lorentz force **F** is exerted on the electron in the damping wiggler as

$$\mathbf{F} = q\,\mathbf{v} \times \mathbf{B}, \tag{19}$$

where **F** is the force, q is the charge, **v** is the velocity vector and **B** is the magnetic field. The time variable is usually replaced by the position variable z along the longitudinal coordinate. With the constant-velocity approximation, the left-hand side of the equation (19) becomes

$$\mathbf{F} = \frac{d\mathbf{p}}{dt} = \frac{d\gamma m\mathbf{v}}{dt} \simeq \gamma m v_z^2 \frac{d^2\mathbf{r}}{dz^2} = \gamma m v_z^2 x'',$$

where γ is the Lorentz factor, m is the mass, **r** is a position vector, x' is dx/dz and $v_z = dz/dt$.

From now on, a prime denotes the derivative with respect to z. The right-hand side of equation (19) becomes

$$F_x = -e\,\mathbf{v} \times \mathbf{B} = ev_z B_y,$$

where e is the charge on an electron.

Assuming that the longitudinal momentum is much larger than the transverse momentum, then the horizontal equation of motion is

$$x'' = \frac{e}{\gamma m v_z} B_y \simeq \frac{e}{p} B_y = \frac{e}{(1+\delta)p_0} B_y \simeq (1-\delta)\frac{e}{p_0} B_y$$
$$= (1-\delta)\frac{B_y}{B_w \rho_w} \quad \left(\frac{e}{p_0} = \frac{1}{B\rho}\right), \tag{20}$$

where p is the magnitude of the momentum, p_0 is the reference momentum, $B\rho$ is the magnetic rigidity, and $\delta = (p - p_0)/p_0$.

Inserting equation (18) into equation (20) with the condition that δ is zero yields

$$x''_{\text{ref}} = \frac{1}{\rho_w} \sin k_w z. \tag{21}$$

When $\delta = 0$, x is a reference orbit. By solving the differential equation, x can be obtained as

$$x_{\text{ref}} = -\frac{1}{\rho_w k_w^2} \sin k_w z. \tag{22}$$

When $\delta \neq 0$, the orbit has an energy-dependent deviation from the reference orbit. The equation of motion is similar to equation (21),

$$x'' = (1-\delta)\frac{1}{\rho_w} \sin k_w z. \tag{23}$$

Solving the differential equation (23) yields

$$x = x_{\text{ref}} + \left(\frac{1}{\rho_w k_w^2} \sin k_w z\right)\delta. \tag{24}$$

The definition of the dispersion is given by

$$x = x_{\text{ref}} + \eta\delta. \tag{25}$$

Comparing equations (24) and (25), the dispersion function can be expressed as

$$\eta = \frac{1}{\rho_w k_w^2} \sin k_w z. \tag{26}$$

The normalized quadrupole strength k_1 should be expressed with z. The definition of k_1 is

$$k_1 = \frac{1}{B_w B\rho}\frac{dB_y}{d\xi}. \tag{27}$$

The slope of ξ is perpendicular to the slope of the tangent line. The slope of the tangent line to the curve is $dx/dz = x'$. The product of x' and $d\xi/dz$ is -1 ($d\xi/dz \times x' = -1$), because they are perpendicular to each other. Then equation (27) becomes

$$k_1 = \frac{1}{B_w \rho_w}\frac{dB_y/dz}{d\xi/dz} = \frac{1}{B_w \rho_w}\frac{dB_y/dz}{-1/x'} = -\frac{1}{B_w \rho_w} x' \frac{dB_y}{dz}. \tag{28}$$

Inserting equations (18) and (22) into (28) yields k_1 as

$$k_1 = \frac{1}{\rho_w^2} \cos^2 k_w z. \tag{29}$$

Lastly, the bending radius is rewritten with the variable z. It is related to the magnetic field as

$$\frac{1}{\rho} = \frac{B_y}{B_w \rho_w} = \frac{B_w \sin k_w z}{B_w \rho_w} = \frac{1}{\rho_w} \sin k_w z. \qquad (30)$$

The damping wiggler contribution to a synchrotron integral will be denoted by the sub-index wig. The integration is from the entrance of the wiggler to the exit of the wiggler, *i.e.* for wiggler L_w. By inserting equations (26), (29) and (30) into the synchrotron integrals, the contributions of the damping wiggler to the synchrotron integrals can be obtained as

$$I_{1,\text{wig}} = \int_0^{L_w} dz \, \frac{\eta}{\rho} = \frac{\lambda_w^2 B_w^2 L_w}{8\pi^2 (B\rho)^2},$$

$$ZI_{2,\text{wig}} = \int_0^{L_w} dz \, \frac{1}{\rho^2} = \frac{B_w^2 L_w}{2(B\rho)^2},$$

$$I_{3,\text{wig}} = \int_0^{L_w} dz \, \frac{1}{|\rho^3|} = \frac{4 B_w^3 L_w}{3\pi (B\rho)^3},$$

$$I_{4,\text{wig}} = \int_0^{L_w} dz \, \frac{\eta}{\rho} \left(\frac{1}{\rho^2} + 2k_1 \right) = \frac{5\lambda_w^2 B_w^4 L_w}{32\pi^2 (B\rho)^4},$$

where β_x is the average value of the horizontal beta function from $z = 0$ to $z = L_w$ and α_x, β_x and γ_x are the Twiss functions. The calculation of $I_{5,\text{wig}}$ uses an approximation

$$\gamma_x \eta^2 + 2\alpha_x \eta \eta' + \beta_x \eta'^2 \simeq \beta_x \eta'^2.$$

Usually $\eta/\eta' \simeq 1/k_w \ll 1$ m. For example, when the wiggler wavelength is 12.57 cm, $1/k_w = 5 \times 10^{-3}$ m. An assumption is also used: that β_x changes smoothly in the damping wiggler, so the integral of $\beta_x \eta'^2 / |\rho^3|$ is approximately the same as the product of β_x and the integrals of $\eta'^2 / |\rho^3|$. Generally, the synchrotron radiation integrals are defined in a curve-linear coordinate. Here the synchrotron radiation integrals are integrated with z; they cannot represent the ring parameters related to path length. For example, $I_{1,\text{wig}}$ does not represent the contribution of the damping wiggler to a momentum compaction factor. Then the new synchrotron radiation integrals

$$I_{1\,\text{new,wig}} = \int_0^{L_w} dz \, x'_\text{ref} \eta' = -\frac{\lambda_w^2 B_w^2 L_w}{8\pi^2 (B\rho)^2},$$

$$I_{4\,\text{new,wig}} = \int_0^{L_w} dz \, \frac{x'_\text{ref} \eta'}{\rho^2} = -\frac{3\lambda_w^2 B_w^4 L_w}{32\pi^2 (B\rho)^4}$$

are defined to denote the ring parameters appropriately. With these new parameters, the damping wiggler contribution to the momentum compaction is expressed as $\alpha_{c,\text{wig}} = I_{1,\text{wig}}/C$.

Acknowledgements

We thank H. Wiedemann for providing helpful information and many useful discussions.

References

APS (2020). *APS Upgrade*, https://www.aps.anl.gov/APS-Upgrade.

Bjorken, J. D. & Mtingwa, S. K. (1983). *Part. Accel.* **13**, 115–143.

Borland, M. (2000). *Elegant: A Flexible SDDS-Compliant Code for Accelerator Simulation.* Technical Report LS-287. Advanced Photon Source, Argonne, IL, USA.

Borland, M., Decker, G., Emery, L., Sajaev, V., Sun, Y. & Xiao, A. (2014). *J. Synchrotron Rad.* **21**, 912–936.

Cai, Y., Ding, Y., Hettel, R., Huang, Z., Wang, L. & Xiao, L. (2013). *An X-ray Free Electron Laser Driven by an Ultimate Storage Ring.* Report SLAC-PUB-15380. SLAC National Accelerator Laboratory, Menlo Park, California, USA.

Deb, K. (2001). *Multi-Objective Optimization Using Evolutionary Algorithms.* Chichester: John Wiley & Sons.

Helm, R. H., Lee, M. J., Morton, P. L. & Sands, M. (1973). *IEEE Trans. Nucl. Sci.* **20**, 900–901.

Huang, Z., Ding, Y. & Schroeder, C. B. (2012). *Phys. Rev. Lett.* **109**, 204801.

Katoh, M. & Kamiya, Y. (1987). *Proceedings of the 1987 IEEE Particle Accelerator Conference*, 16–19 March 1987, Washington DC, USA, Vol. 1, pp. 437–439.

Liu, L., Milas, N., Mukai, A. H. C., Resende, X. R., Rodrigues, A. R. D. & de Sá, F. H. (2013). *Proceedings of the Fourth International Particle Accelerator Conference (IPAC2013)*, 12–17 May 2013, Shanghai, China, pp. 1874–1876. TUPWO001.

Luong, V. (2018). *EUV Lithography*, https://eng.kuleuven.be/en/research/phd/arenberg-youngster-seminars/ays-pdf/20180516-luong-ays-final.pdf.

MAX IV (2010). *MAX IV DDR – The MAX IV Detailed Design Report*, https://www.maxiv.lu.se/accelerators-beamlines/accelerators/accelerator-documentation/max-iv-ddr/.

Revol, J.-L. (2017). *ESRF-EBS: The Extremely Brilliant Source Project*, http://indico.psi.ch/conferenceDisplay.py?confId=5589.

Riemann, B. & Streun, A. (2019). *Phys. Rev. Accel. Beams*, **22**, 021601.

Shin, S., Kwon, S., Kim, D.., Kim, D.., Kim, M., Kim, S.., Kim, S.., Kim, J., Kim, C., Park, B., Park, S.., Park, S.., Park, E., Son, Y., Yoon, J., Lee, B., Lee, E., Lee, J.., Lee, H.., Joo, Y., Choi, J., Ha, T., Hwang, W., Hwang, I., Lee, J.., Oh, B., Lee, C., Lee, H.., Kim, J.., Hwang, J. Y., Nam, S. H. & Cho, M. (2013). *J. Instrum.* **8**, P01019.

SPring-8 (2014). *SPring-8-II Conceptual Design Report*, http://rsc.riken.jp/eng/pdf/SPring-8-II.pdf.

Steier, C., Byrd, J. M., De Santis, S., Nishimura, H., Robin, D., Sannibale, F., Sun, C., Venturini, M. & Wan, W. (2016). *Proceedings of the 7th International Particle Accelerator Conference (IPAC2016)*, 8–13 May 2016, Busan, Korea, pp. 2956–2958. WEPOW049.

Walker, R. P. (1995). *CAS – CERN Accelerator School: 5th Advanced Accelerator Physics Course*, 20 September–1 October 1993, Rhodes, Greece, pp. 807–835.

Wiedemann, H. (1988). *Nucl. Instrum. Methods Phys. Res. A*, **266**, 24–31.

Wiedemann, H. (1993). *Particle Accelerator Physics I.* Berlin: Springer.